

# Numerical simulation of the inception of channel meandering

Jennifer G. Duan<sup>1\*</sup> and Pierre Y. Julien<sup>2</sup>

<sup>1</sup> Division of Hydrologic Sciences, Desert Research Institute, 755 E. Flamingo Road, Las Vegas, Nevada 89119, USA

<sup>2</sup> Engineering Research Centre, Colorado State University, Fort Collins, CO 80523, USA

\*Correspondence to: J. G. Duan,  
Division of Hydrologic Sciences,  
Desert Research Institute,  
University and College System of  
Nevada, 755 E. Flamingo Road,  
Las Vegas, NV 89119, USA.  
E-mail: gduan@dri.edu

## Abstract

The inception of channel meandering is the result of the complex interaction between flow, bed sediment, and bank material. A depth-averaged two-dimensional hydrodynamic model is developed to simulate the inception and development of channel meandering processes. The sediment transport model calculates both bedload and suspended load assuming equilibrium sediment transport. Bank erosion consists of two interactive processes: basal erosion and bank failure. Basal erosion is calculated from a newly derived equation for the entrainment of sediment particles by hydrodynamic forces. The mass conservation equation, where basal erosion and bank failure are considered source terms, was solved to obtain the rate of bank erosion. The parallel bank failure model was tested with the laboratory experiments of Friedkin on the initiation and evolution processes of non-cohesive meandering channels. The model replicates the downstream translation and lateral extension of meandering loops reasonably well. Plots of meandering planforms illustrate the evolution of sand bars and redistribution of flow momentum in meandering channels. This numerical modelling study demonstrates the potential of depth-integrated two-dimensional models for the simulation of meandering processes. Copyright © 2005 John Wiley & Sons, Ltd.

**Keywords:** meandering channel; sediment transport; numerical model; bank erosion

Received 1 September 2004;  
Revised 28 February 2005;  
Accepted 17 March 2005

## Introduction

The lateral migration of meandering channels, involving the complex mechanism of fluid dynamics, sediment transport and bank erosion, has intrigued geomorphologists and river engineers for decades. Starting from straight channels, alternate bars and pools form, which further enhances the initiation of meandering. Flow converges to the concave banks and diverges at the convex banks due to the centrifugal force that generates a spiral flow in meandering channels. Flow momentum redistribution causes bed degradation near concave banks and deposition near convex banks. Bed degradation steepens concave banks whereas deposition stabilizes convex banks. This causes concave banks to retreat as bank erosion occurs, while convex banks advance with the build-up of point bars. Therefore, the migration of meandering channels is accompanied with an increase in meandering amplitude and wavelength, downstream translation, lateral extension, rotation, and formation of chute cutoffs.

To model the formation or evolution of meanders, both process-based (Ikeda *et al.*, 1981; Ikeda and Nishimura, 1986) and physically based (Osman and Thorne, 1988) bank erosion models are feasible. Process-based models assume a rate of bank erosion proportional to near-bank flow velocity. In contrast, physically based models calculate sediment transport and bank erosion rates to determine the advance and retreat of channel bankline. However, the erosion coefficient in process-based models is empirical and does not reflect bank geometry and bank material at specific locations in natural meanders. Process-based models can be effective in predicting the long-term behaviour of meandering rivers (Parker and Andrews, 1986; Sun *et al.*, 1996; Lancaster and Bras, 2002). Physically based models can be specifically used to determine the rate of bank erosion at individual locations within a natural meandering channel by knowing the flow field, bank geometry and bank material. They are expected to become more successful in predicting immediate or short-term geomorphic responses to river modifications.

With the rapid development of mathematical models and recent advances in computer technology, two- and three-dimensional computational fluid dynamic (CFD) models have become increasingly popular to simulate morphodynamic processes of natural rivers, meandering streams (Mosselman, 1998; Duan *et al.*, 2001; Olsen, 2003), and braiding

channels (Nicholas and Smith, 1999). Mosselman (1998) added a bank erosion model to a two-dimensional, depth-averaged model and applied it to the Ohre River, a meandering gravel-bed river in the former state of Czechoslovakia. Poor agreement between modelling results and observations were ascribed to the shortcomings of the flow model rather than to the bank erosion subroutines. Duan *et al.* (2001) solved the two-dimensional, depth-averaged momentum and continuity equations expressed in Cartesian coordinates for the flow field. The secondary flow-correction term (Engelund, 1974) was then implemented to redirect the transport of bedload sediment from the calculated depth-averaged velocity. A new bank erosion model derived from the mass conservation law for near-bank cells was employed to simulate the migration of bank lines. The simulated initiation, migration and evolution of a meander indicated that the rate of bank erosion is a function of longitudinal gradient in sediment transport, strength of secondary flow, and mass wasting from bank erosion. Although sediment transport and basal bank erosion were considered, the geotechnical bank failure of cohesive bank material following basal erosion was neglected (Duan *et al.*, 2001). As a result, the simulated meandering wavelength and amplitude did not agree with the observations described in Friedkin (1945).

Darby *et al.* (2002) replaced the bank erosion subroutine within the two-dimensional, depth-averaged numerical model RIPA with a new physically based bank erosion model. Within this algorithm, basal erosion of cohesive bank material and subsequent bank failure as well as transport and deposition of eroded bank material were simulated to predict the evolution of meandering channels. The rate of basal erosion of cohesive material was obtained by applying a simple model (ASCE Task Committee, 1998) where the rate of basal erosion is an exponential function of the excessive shear stress. The mass volume of bank failure was calculated from the bank erosion model for cohesive bank material (Osman and Thorne, 1988). Then, the eroded bank material was divided into three groups according to grain size, and transported or deposited at bank toes as bedload or suspended load. The variation of coarse and fine sediments in sand bars was simulated with sediment transport calculations by size fractions. When the effects of secondary current on sediment transport were considered theoretically or empirically, the two-dimensional, depth-averaged hydrodynamic model combined with the sediment transport and bank erosion models became capable of modelling the evolutionary processes of meandering channels.

A full three-dimensional (3D) CFD model having the solutions of flow velocity in three dimensions has been applied successfully to simulate the formation of meandering streams in the laboratory (Olsen, 2003). A 3D CFD model can provide a flow field that is three-dimensional so that the secondary flow correction is not needed. Advances in the numerical scheme and computer resources potentially will reduce significantly the computational time. Olsen (2003) also stated that another advantage in using the 3D CFD model lies in its capability to simulate the morphodynamic process without a separate bank erosion model because a bank erosion model is not required when the entire basin is chosen as the computational domain.

This study presents a two-dimensional numerical model that links a physically based bank erosion model with the bend migration model to simulate the formation process of meandering channels. The developed model encompasses: a depth-averaged, two-dimensional flow hydrodynamic model; a sediment transport model; and a bank erosion model. The flow hydrodynamic model simulating flow and mass dispersion in meandering channels is described in more details in Duan (2004). New components specific to this study include: (1) the direction of bedload transport is determined by combining the effects of secondary flow and transverse bed slope; and (2) the bank line retreat and advance can be calculated from near-bank mass conservation where bank material from basal erosion and bank failure are treated as source terms. This paper emphasizes the development and application of the sediment transport and bank erosion models. The goal of this simulation is to illustrate the modelling approach with potential applications to natural streams.

## Flow Simulation

The governing equations for flow simulation are the depth-averaged Reynolds approximation of momentum equations (Equations 1 and 2) and continuity equation (Equation 3).

$$\frac{\partial(h\bar{u})}{\partial t} + \frac{\partial}{\partial x}(h\bar{u}^2) + \frac{\partial D_{uu}}{\partial x} + \frac{\partial}{\partial y}(h\bar{u}\bar{v}) + \frac{\partial D_{uv}}{\partial y} = -gh\frac{\partial\zeta}{\partial x} + \frac{\partial}{\partial x}(h\tau_{xx}) + \frac{\partial}{\partial y}(h\tau_{xy}) - \tau_{bx} \quad (1)$$

$$\frac{\partial(h\bar{v})}{\partial t} + \frac{\partial}{\partial x}(h\bar{u}\bar{v}) + \frac{\partial D_{uv}}{\partial x} + \frac{\partial}{\partial y}(h\bar{v}^2) + \frac{\partial D_{vv}}{\partial y} = -gh\frac{\partial\zeta}{\partial y} + \frac{\partial}{\partial x}(h\tau_{yx}) + \frac{\partial}{\partial y}(h\tau_{yy}) - \tau_{by} \quad (2)$$

$$\frac{\partial h}{\partial t} + \frac{\partial}{\partial x}(h\bar{u}) + \frac{\partial}{\partial y}(h\bar{v}) = 0 \quad (3)$$

where  $\bar{u}$  and  $\bar{v}$  are depth-averaged velocity components in  $x$  and  $y$  directions, respectively;  $t$  is time;  $\zeta$  is surface elevation;  $h$  is flow depth;  $g$  is acceleration due to gravity;  $\tau_{bx}$  and  $\tau_{by}$  are friction shear stress terms at the bottom in  $x$  and  $y$  directions, respectively, written as

$$\tau_{bx} = \frac{n^2 g}{h^{\frac{1}{3}}} \bar{u} U \quad \text{and} \quad \tau_{by} = \frac{n^2 g}{h^{\frac{1}{3}}} \bar{v} U$$

in which  $U$  is depth-averaged total velocity and  $n$  is Manning's roughness coefficient;  $\tau_{xy}$ ,  $\tau_{xx}$ ,  $\tau_{yx}$  and  $\tau_{yy}$  are Reynolds stress terms, which are expressed as

$$\tau_{xx} = 2v_t \frac{\partial \bar{u}}{\partial x}, \quad \tau_{yy} = 2v_t \frac{\partial \bar{v}}{\partial y}, \quad \tau_{xy} = \tau_{yx} = v_t \left( \frac{\partial \bar{u}}{\partial y} + \frac{\partial \bar{v}}{\partial x} \right)$$

in which  $v_t$  is eddy viscosity; and  $D_{uu}$ ,  $D_{uv}$  and  $D_{vv}$  are dispersion terms resulting from the discrepancy between the depth-averaged velocity and the actual velocity, expressed as

$$D_{uu} = \int_{z_0}^{z_0+h} (u - \bar{u})^2 dz, \quad D_{uv} = \int_{z_0}^{z_0+h} (u - \bar{u})(v - \bar{v}) dz, \quad D_{vv} = \int_{z_0}^{z_0+h} (v - \bar{v})^2 dz \quad (4)$$

where  $z_0$  is zero velocity level.

The depth-averaged parabolic eddy viscosity model is adopted, where the depth-averaged eddy viscosity is obtained as

$$v_t = \frac{1}{6} \kappa u_* h \quad (5)$$

where  $u_*$  is shear velocity and  $\kappa$  is von Karman's constant.

To include the effect of secondary flow, four dispersion terms were added to the momentum equations. To derive the mathematical expressions of these terms, we assumed that the streamwise velocity satisfies the logarithmic law, and then the streamwise velocity profile can be written as

$$\frac{u_l}{\bar{u}_l} = \frac{\ln\left(\frac{z}{z_0}\right)}{\frac{z_0}{h} - 1 + \ln\left(\frac{h}{z_0}\right)} \quad (6)$$

where  $z$  is vertical coordinate;  $u_l$  and  $\bar{u}_l$  are the streamwise and depth-averaged velocity, respectively; and  $u_*$  is shear velocity, and  $z_0$  was calculated according to flow hydraulic smooth, transition and rough regimes.

The transverse velocity profile of the secondary flow is assumed to be linear. The profile of the transverse velocity proposed by Odgaard (1989a) was adopted in this model.

$$v_r = \bar{v}_r + 2v_s \left( \frac{z}{h} - \frac{1}{2} \right) \quad (7)$$

where  $v_r$ ,  $\bar{v}_r$  and  $v_s$  are the transverse velocity, the depth-averaged transverse velocity, and the transverse velocity at the water surface, respectively. Engelund (1974) derived the deviation angle of the bottom shear stress and gave that

$$\left( \frac{\tau_r}{\tau_l} \right)_b \approx \left( \frac{v_r}{u_l} \right)_b = 7.0 \frac{h}{r} \quad (8)$$

where  $r$  is the radius of channel curvature. According to Equation 7, the secondary flow velocities at the surface and the bottom are equal. Therefore, Equation 8 (Engelund, 1974) was used as the transverse velocity at the surface. The dispersion terms at the streamwise and transverse directions can be expressed as

$$D_{uu}^c = \int_{z_0}^{z_0+h} (u_l - \bar{u}_l)^2 dz, \quad D_{uv}^c = \int_{z_0}^{z_0+h} (u_l - \bar{u}_l)(v_r - \bar{v}_r) dz, \quad D_{vv}^c = \int_{z_0}^{z_0+h} (v_r - \bar{v}_r)^2 dz \quad (9)$$

where  $D_{uu}^c$ ,  $D_{uv}^c$ , and  $D_{vv}^c$  denote dispersion terms in curvilinear coordinates. Substituting Equations 6, 7 and 8 into the above dispersion terms yields

$$D_{uu}^c = \chi^2 \bar{u}_l^2 h [-\eta_0 \ln \eta_0 (\ln \eta_0 - 2) + 2\eta_0 (1 - \eta_0) (1 - \ln \eta_0) - (\eta_0 - 1)^3] \quad (10)$$

$$D_{uv}^c = 49.0 \bar{u}_l^2 \frac{h^3}{r^2} \left[ -\frac{1}{3} \eta_0^3 + \frac{1}{2} \eta_0^2 - \frac{1}{4} \eta_0 + \frac{1}{12} \right] \quad (11)$$

$$D_{vv}^c = 3.5 \bar{u}_l^2 \frac{h^2}{r} \left[ -\eta_0^2 \ln \eta_0 + \eta_0 \ln \eta_0 - \eta_0 + \eta_0^3 \right] \quad (12)$$

where  $\chi = 1/(\eta_0 - 1 - \ln \eta_0)$  and  $\eta_0 = z_0/h$  is the dimensionless zero bed elevation. If  $\theta_l$  denotes the angle between the streamwise direction and the positive  $x$ -axis, and  $\theta_n$  is the angle between the transverse direction pointing to the outer bank and the positive  $x$ -axis, the depth-averaged velocities in curvilinear coordinates can be converted to those in Cartesian coordinates according to the following equations

$$\bar{u} = \bar{u}_l \cos \theta_l + \bar{v}_r \cos \theta_n \quad \bar{v} = \bar{u}_l \sin \theta_l + \bar{v}_r \sin \theta_n \quad (13)$$

Then, the dispersion terms in Cartesian coordinates can be correlated to those in curvilinear coordinates as follows

$$D_{uu} = D_{uu}^c \cos^2 \theta_l + 2D_{uv}^c \cos \theta_l \cos \theta_n + D_{vv}^c \cos^2 \theta_n \quad (14)$$

$$D_{vv} = D_{uu}^c \sin^2 \theta_l + 2D_{uv}^c \sin \theta_l \sin \theta_n + D_{vv}^c \sin^2 \theta_n \quad (15)$$

$$D_{uv} = D_{uu}^c \cos \theta_l \sin \theta_l + D_{uv}^c (\cos \theta_n \sin \theta_l + \sin \theta_n \cos \theta_l) + D_{vv}^c \sin \theta_n \cos \theta_n \quad (16)$$

These dispersion terms were included in Equations 1 and 2 to solve for flow velocity. A more detailed description of the hydrodynamic model is given in Duan (2004).

## Sediment Transport Simulation

### Bedload transport

To predict bedload transport in a curved channel, at least three forces should be considered. These forces include bed shear stress due to longitudinal flow, bed shear stress due to curvature-induced secondary flow in the transverse direction, and component of gravitational force on the slope of the channel bed or bank. The influence of gravity on bedload transport is reflected in its effect on incipient motion of sediment and direction of bedload transport.

Numerous equations are available to predict the transport rate of bedload sediment. The present study selected the Meyer-Peter and Muller bedload transport formula that is valid for uniform sediment with a mean particle size ranging from 0.23 to 28.6 mm. In this research, the bedload transport rate is computed by this formula as follows

$$q_b = C_m [(s - 1)g]^{0.5} d_{50}^{1.5} (\mu' \tau_* - \tau_{*c})^{1.5} \quad (17)$$

where  $q_b$  is the total bedload transport rate per unit width;  $\tau_* = (\rho u_*^2)/[(\rho_s - \rho)gd_{50}]$  is the effective particle mobility parameter;  $\tau_{*c} = \tau_c/[(\rho_s - \rho)gd_{50}]$  is the critical value of  $\tau_*$  for incipient motion depending on particle Reynolds number ( $R_*^* = (u_* d_{50})/\nu$ ), and  $\tau_{*c} = 0.047$  when  $R_*^* > 100$ ; constant coefficient  $C_m = 8.0$ ; and the bed-form effect was ignored so that the factor  $\mu'$  was omitted in this model;  $d_{50}$  is the mean particle diameter;  $s = \rho_s/\rho$ , where  $\rho_s$  and  $\rho$  are densities of sand and water, respectively.

Bedload transport is known to deviate from the downstream flow direction because of the influence of the secondary flow and bed-transverse slope. The deviation angle is defined as the angle between the centreline of the channel and the direction of shear force at the bed. Engelund (1974), Kikkawa *et al.* (1976), Parker (1984), Bridge (1992) and Darby and Delbono (2002) derived relations to estimate the deviation angle based on the analytical solutions of flow field in sinuous channels. Among them, Bridge (1992) and Darby and Delbono (2002) stressed that flow in the bend with a varying curvature is non-uniform, so steady and non-uniform flow momentum equations are necessary when solving the flow field. As a result, the tangent of the deviation angle (Darby and Delbono, 2002) is not only a function

of the mean longitudinal and transverse velocity components, local radius of the curvature and friction, but also varies spatially in the sine-generated bends. This study adopted the angle of deviation,  $\beta$ , derived by Ikeda (1989)

$$\tan \beta = \frac{u_{bn}}{u_{bs}} - \frac{1 + \alpha\mu}{\lambda_s\mu} \sqrt{\frac{\tau_{*c}}{\tau_*}} \frac{\partial z_b}{\partial n} = -N_* \frac{h}{r} - \frac{1 + \alpha\mu}{\lambda_s\mu} \sqrt{\frac{\tau_{*c}}{\tau_*}} \frac{\partial z_b}{\partial n} \quad (18)$$

where  $u_{bn}$  and  $u_{bs}$  are the transverse and longitudinal velocities near the bed;  $\alpha = 0.85$ ,  $\mu = \tan \phi$  and  $\lambda_s = 0.59$  are friction coefficients, in which  $\phi$  is the angle of repose;  $r$  is the radius of curvature;  $N_*$  is a coefficient that equals 7.0 derived by Engelund (1974); and  $\partial z_b / \partial n$  denotes the transverse slope. The first term on the right of Equation 18 accounts for the effect of secondary flow velocity at the bottom, and the second term quantifies the effect of the transverse slope. The components of bedload transport in  $x$  and  $y$  directions of Cartesian coordinates can be obtained as

$$\begin{cases} q_{bx} = q_b \cos(\theta_t - \beta) \\ q_{by} = q_b \sin(\theta_t - \beta) \end{cases} \quad (19)$$

where  $q_{bx}$  and  $q_{by}$  are components of bedload transport rate in  $x$  and  $y$  directions, respectively; and  $\theta_t$  is the angle between the centreline and positive  $x$  axis as defined in the flow model.

The gravity component facilitates or impedes the motion of sediment particles resting on a sloping bed because gravity may or may not work in the same direction as the fluid shear force. Van Rijn (1989) proposed a formula to account for this slope effect. In the case of a longitudinal sloping bed (in the bed-shear stress direction), the critical shear stress  $\tau_{*c}$  is written as

$$\tau_{*c} = K_1 \tau_{*c,0} \quad (20)$$

where  $\tau_{*c,0}$  is the critical mobility parameter on a horizontal bottom, which can be predicted from Shield's curve. The coefficient  $K_1$  is defined as

$$K_1 = \sin(\phi - \beta_1) / \sin \phi \quad (\text{for a downsloping bed}) \quad (21)$$

$$K_1 = \sin(\phi + \beta_1) / \sin \phi \quad (\text{for an upsloping bed}) \quad (22)$$

where  $\phi$  is the angle of repose; and  $\beta_1$  is the longitudinal bed-slope angle. This formulation has been developed by Bormann and Julien (1990). In the case of a transverse sloping bed, the critical bed shear stress is

$$\tau_{*c} = K_2 \tau_{*c,0} \quad (23)$$

where  $K_2 = [\cos \beta_2][1 - (\tan^2 \beta_2 / \tan \phi)]^{0.5}$ , and  $\beta_2$  is the transversal bed-slope angle. This formulation is attributed to Lane, as recently described in Julien (2002). For a combined longitudinal and transversal bed slope, the following relation is used:

$$\tau_{*c} = K_1 K_2 \tau_{*c,0} \quad (24)$$

## Suspended load transport

To calculate the rate of suspended sediment transport, a suspended sediment concentration profile must be assumed. In this model, the classic Rouse profile (van Rijn, 1989) is assumed to be valid at  $z = a$  from the channel bed to the water surface. The Rouse profile is written as

$$\frac{C}{C_a} = \left( \frac{h - z}{z} \frac{a}{h - a} \right)^Z \quad (25)$$

where  $a$  is the reference bed level;  $z$  is the distance from the bottom;  $Z$  is the Rouse number; and  $C$  and  $C_a$  are concentrations of suspended sediment and its value at  $z = a$ , respectively. The expression of the Rouse number is given as

$$Z = \frac{\omega}{\kappa \beta' u_*} \quad (26)$$

where  $\omega$  is the falling velocity;  $\kappa = 0.4$  is von Karman's constant;  $u_*$  is the shear velocity, and  $\beta'$  describes (van Rijn, 1989) the difference in the diffusion of a sediment particle from the diffusion of a fluid 'particle'. The coefficient  $\beta'$  is calculated as

$$\beta' = 1 + 2 \left( \frac{\omega}{u_*} \right)^2; \quad 0.1 < \frac{\omega}{u_*} < 1 \quad (27)$$

The suspended sediment transport rate is the product of the velocity profile and the suspended sediment concentration profile. The longitudinal velocity profile satisfies the logarithmic law and is expressed in Equation 6. The transverse velocity profile of the secondary flow was assumed to be linear and satisfied Equation 7. The right-hand side of Equation 7 has two terms: one is the depth-averaged secondary flow velocity relating to bed topography, and the other has a zero value if integrating over flow depth.

The van Rijn (1989) formula was adopted here for computing the reference concentration

$$C_a = 0.015 \frac{d_{50}}{a} \frac{T^{1.5}}{D_*^{0.3}} \quad (28)$$

where

$$D_* = d_{50} \left[ \frac{(s-1)g}{\nu^2} \right]^{\frac{1}{3}}$$

is the dimensionless particle diameter;

$$T = \frac{\tau_* - \tau_{*c}}{\tau_{*c}} \quad (29)$$

where  $\tau_*$  is the dimensionless grain shear stress parameter, and  $\tau_{*c}$  is the critical bed-shear stress according to Equation 24. Knowing the longitudinal and transverse velocity profiles (Equations 6 and 7) and the concentration of suspended sediment (Equation 25), the suspended sediment transport rates in the longitudinal and transverse directions can be obtained as

$$q_{sl} = \int_{z_0}^h u_l C dz; \quad q_{sr} = \int_{z_0}^h v_r C dz \quad (30)$$

where  $q_{sl}$  and  $q_{sr}$  are the suspended sediment transport rates in the longitudinal and transverse directions, respectively. Because the Cartesian coordinates are used in this model, the longitudinal and transversal components of the suspended sediment transport rate were transformed into the  $x$  and  $y$  components of the Cartesian coordinates through the following equations

$$q_{sx} = q_{sl} \cos \theta_l + q_{sr} \cos \theta_r \quad (31)$$

$$q_{sy} = q_{sl} \sin \theta_l + q_{sr} \sin \theta_r \quad (32)$$

where  $\theta_l$  and  $\theta_r$  are the angles defined in Equation 13, and  $q_x$  and  $q_y$  are the total suspended loads in  $x$  and  $y$  directions, respectively.

## Computation of bed-elevation change

The sediment continuity equation is then used for calculating bed-elevation changes

$$(1-p) \frac{\partial z_b}{\partial t} + \frac{\partial(q_{bx} + q_{sx})}{\partial x} + \frac{\partial(q_{by} + q_{sy})}{\partial y} = 0 \quad (33)$$

where  $p$  is the porosity of the bed and bank material, and  $z_b$  is the bed elevation.

## Bank Erosion Simulation

Bank erosion consists of two interactive physical processes: basal erosion and bank failure (Osman and Thorne, 1988; Darby and Thorne, 1996). Basal erosion refers to the fluvial entrainment of bank material by flow-induced forces that act on the bank surface: drag force, resistance force, and lift force. Bank failure occurs due to geotechnical instability (e.g. planar failure, rotational failure, sapping or piping). Bank erosion does not guarantee the retreat of bank line because the eroded bank material may be deposited close to the banks. The rate of bank erosion traditionally is calculated empirically from the geometry of channel bends, bank material, and flow intensity (Hooke, 1995). Process-based bend migration models (Ikeda *et al.*, 1981; Johannesson, 1985; Odgaard, 1989a,b; Crosato, 1990; Sun *et al.*, 2001a,b) were successfully applied for long-term trends in meandering evolution. Although the rate of bank erosion can be proportional to near-bank excess velocity, however, this assumption could be unrealistic if eroded bank material is deposited as sand bars.

The present model separates the calculation of bank erosion and the advance and retreat of bank lines. Sediment from basal erosion is calculated by using an analytical approach derived in Duan (2001). Mass wasting from bank failure is calculated using the parallel bank failure model for non-cohesive bank material. The contributions of sediment from basal erosion and bank failure are considered as source terms for sediment continuity, and then advance or retreat of bank lines are determined by solving the near-bank mass conservation equation. The present model adopts a simple bank-failure model similar to the slumping bank-failure model.

### Basal erosion

Basal erosion entrains bank material under the water surface. The rate of basal erosion is the rate of bank material entrainment to the water body per unit channel length per unit time. The depth-averaged bank erosion rate is determined as the difference between the entrainment and deposition of bank material expressed as follows in Duan (2001)

$$\bar{\xi} = \sin \bar{\beta} \sqrt{\frac{C_L}{3\rho_s}} \left( 1 - \frac{C}{C_*} \cos \bar{\beta} \right) \left( 1 - \frac{\tau_{bc}}{\tau_{b0}} \right)^{\frac{3}{2}} \sqrt{\tau_{b0}} \quad (34)$$

where  $\bar{\beta}$  is the averaged bank slope;  $\bar{\xi}$  is the depth-averaged bank erosion rate due to hydraulic force; concentrations  $C$  and  $C_*$  are the depth-averaged and equilibrium concentrations of suspended sediment, respectively, such that  $C = C_*$  for equilibrium suspended load transport;  $\rho_s$  is the density of sediment particle;  $C_L$  is the coefficient of lift force ranging from 0.1 to 0.4 depending on the mean grain size of the sand (Chien and Wan, 1991); shear stresses at the toe of the bank slope and critical shear stress for basal erosion are represented as  $\tau_{b0}$  and  $\tau_{bc}$ , respectively. Shear stress at bank toe equals the shear stress acting on the channel bottom,  $\tau$ . If bank material is the same as bed material, such as in Friedkin's (1945) experiment, the critical shear stress of bank material has the same value as that for bed material.

The mass volume contributing to the main channel from basal erosion can be calculated as

$$q_{br}^b = \frac{\bar{\xi}(1-p)h_b}{\sin \bar{\beta}} \quad (35)$$

where  $q_{br}^b$  is the net volume of sediment contributed to the main channel from bank erosion, and  $h_b$  is flow depth at near-bank. To account for the porosity  $p$  of the bank material, the factor  $1-p$  is multiplied at the denominator. If  $\bar{\xi} = 0$ , the riverbank is not undergoing erosion, so the near-bank, suspended sediment concentration reaches the value of equilibrium. The term  $\sin \bar{\beta}$  converts the distance of bank erosion to the volumetric net bank material from basal erosion.

### Mass failure for non-cohesive bank material

Pizzuto (1990) derived and applied a slumping bank-failure model for non-cohesive bank material, which was later modified by Nagata *et al.* (2000). Fluvial erosion degrades the channel bed and destabilizes the upper bank until the bank angle exceeds the angle of repose for bank material. The slumping bank-failure model requires the bank-failure surface to be inclined at the angle of repose projected to the floodplain. It is well suited for the case of non-cohesive sediment, like the laboratory experiments of Friedkin (1945) and Lan (1990).



In natural environments, vegetation, heterogeneity in bank material and pore water pressure will add an apparent cohesion to the original non-cohesive material. The planar bank-failure model (Osman and Thorne, 1988; Darby and Thorne, 1996) is more appropriate as compared to the slumping model. In this study, the slumping bank-failure model was combined with the parallel retreat method. It assumes that mass wasting from bank failure is the product of the rate of basal erosion and height of the bank surface above the water surface. Therefore, the amount of bank material from mass failure is calculated as

$$q_{br}^f = \bar{\xi} \Delta h_{bank} (1 - p) \quad (36)$$

where  $q_{br}^f$  is the sediment material eroded per unit channel width from bank failure, and  $\Delta h_{bank}$  is the bank height above the water surface.

### Advance and retreat of bank lines

Bank erosion eventually causes bank advance or retreat. An advance is caused by the sediment deposition near the bank. The deposited sediment can be supplied from an eroded bank or bed material transported from upstream. A bank retreats as the material is transported away by flow. Predicting bank advance or retreat is based on a balance (or mass conservation) of the sediment in a control volume near the bank, including sediment from bank erosion and failure, sediment stored on the bed due to deposition, and sediment fluxes transported in and out of the control volume. Considering the mass balance within a control volume near the bank (Figure 1), the sediment continuity equation is written as

$$\left( q_l + \frac{\partial q_l}{\partial l} dl \right) \frac{dr}{2} - q_l \frac{dr}{2} + q_r dl - q_{br} dl = -\varepsilon h_b dl \quad (37)$$

where  $\varepsilon$  is the actual bank erosion rate;  $\varepsilon > 0$ ,  $\varepsilon < 0$ , and  $\varepsilon = 0$  correspond to bank advance, retreat, and unchanged, respectively; and  $dr$  is the width of the control volume (Figure 1). Simplifying and eliminating  $dl$  and  $dr$  from both sides of Equation 37 produces

$$\varepsilon = - \frac{\left( \frac{\partial q_l}{\partial l} \frac{dr}{2} + q_r - q_{br} \right)}{h_b} \quad (38)$$

where  $\varepsilon$  is the bank erosion rate (if the bank advances,  $\varepsilon > 0$ ; if the bank retreats,  $\varepsilon < 0$ ; if the bank is unchanged,  $\varepsilon = 0$ );  $dr$  is defined as the width of the control volume nearest to the edge of the bank;  $h_b$  is the near-bank flow depth;  $q_l$  and  $q_r$  are the total sediment transport rates in the longitudinal and transverse directions, respectively; and  $q_{br} = q_{br}^b + q_{br}^f$  is the transversal component of the sediment transport rate at the near-bank region as a result of bank erosion. Under the assumption of a triangular cross-section of the boundary element,  $dr$  in Equation 38 is half the distance from the nearest boundary node to the edge of bank. We can reason from Equation 38 that the bank retreats when the net longitudinal and transverse sediment transport rate is decreased or a net amount of sediment materials are carried out

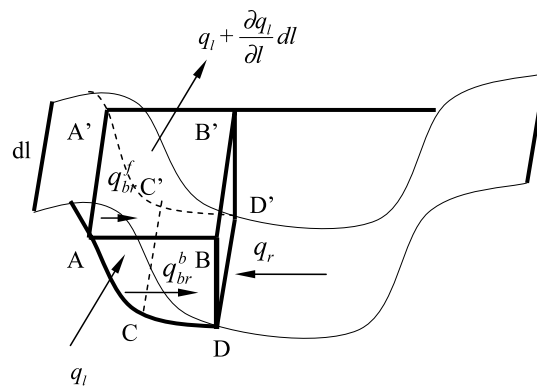


**Figure 1.** Mass balance at near-bank region.



of a control volume near the bank. Conversely, if the net sediment transport to the control volume is increased, the bank will advance. The variable  $dr$  is defined as the width of the control volume adjacent to the bank.

Comparing with the Ikeda *et al.* (1981) bank erosion model, the bank erosion rate in the present study is determined by the flow and sediment conditions near the bank rather than by only excess velocity. Accordingly, the movement of a bank is only related to the near-bank flow field. If the excess near-bank velocity is greater than zero, the bank will retreat. Equation 38 considers sediment transport fluxes, and one can see that even when flow velocity and shear stress near the bank are high, the bank may not retreat, because a net sediment flux may be transporting into the control volume adjacent to the bank.

## Numerical Methods

The 'efficient element method' (Wang and Hu, 1990) is used to solve the momentum and continuity equations. The numerical technique was originally a collocated, weighted residual finite element method. The traditional Lagrangian interpolation function is employed to discretize the linear terms in Equations 1, 2, and 3. To address adequately the upwinding effect, another set of interpolating functions is derived based on the solution of the convection and diffusion equation to discretize non-linear terms (advection terms) in the flow momentum equations. These two sets of shape functions are transformed to the shape function for global elements based on the isoparametric mapping approach. A detailed description of the numerical scheme for the flow hydrodynamic model can be found in Duan (2004).

The sediment continuity equation (Equation 33) is discretized using the Lagrangian interpolation shape functions. A backward finite difference scheme is used for the time derivative term. The discretized form of Equation 33 is

$$(1 - p) \frac{z_b^t - z_b^{t-1}}{\Delta t} + \sum_{i=1}^9 \frac{\partial \varphi_i}{\partial x} q_{xi} + \sum_{i=1}^9 \frac{\partial \varphi_i}{\partial y} q_{yi} = 0 \quad (39)$$

where  $\varphi_i$  is the shape function with the superscription denoting the time step, and the subscription denoting the node number. In the present study, flow and bed deformation computations are decoupled. Sediment transport rates are calculated after flow has reached a steady state. Then, Equation 39 is solved to obtain a new bed elevation. The time step of sediment computation is selected such that bed-elevation changes are less than 2 per cent of the flow depth.

Besides calculating bed-elevation changes, bank lines are also adjusted according to the rate of bank erosion. Figure 2 illustrates the calculation with Equation 38 for the bank advance and retreat rate at the elements adjacent to

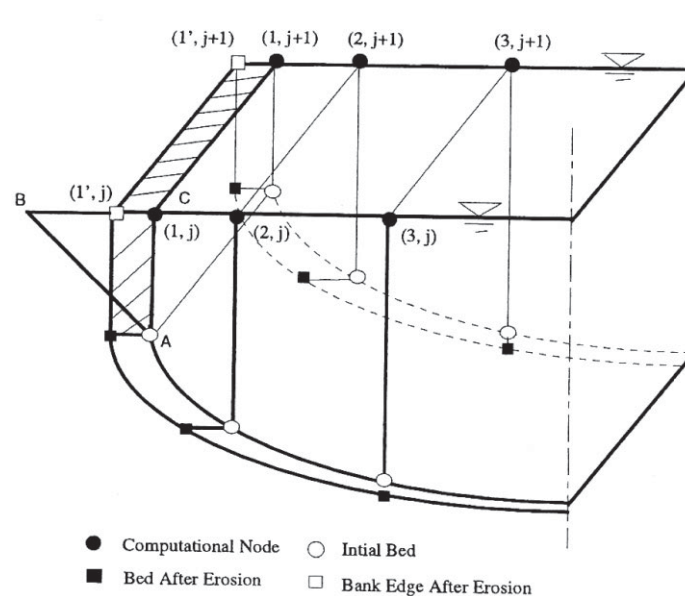


**Figure 2.** Movement of nodes at banks.

the bank. The boundary nodes are  $(1, j)$  and  $(1, j + 1)$ , and the adjacent internal nodes are  $(2, j)$  and  $(2, j + 1)$ . Equation 38 is solved at node  $(1, j)$  to obtain the bank erosion rate at the edge of bank  $B$ . The boundary element used to evaluate the bank erosion rate is a prism-like, three-dimensional element with a triangular cross-section  $ABC$ . The bank erosion rate at node  $(1, j)$  is assumed to be the same as that at the edge of bank  $B$ , which can be expressed as

$$\varepsilon_{i,j} = \frac{\Delta r}{2} \frac{q_l(2, j) - q_l(2, j + 1)}{\Delta l} - q_r(2, j) + q_{br}(1, j) \quad (40)$$

where  $\Delta r$  is the distance between  $B$  and  $C$ . As a boundary condition, the longitudinal component of the sediment transport rate at node  $(1, j)$  is assumed to be the same as the adjacent internal node  $(2, j)$ . Using Equations 35 and 36, the expression  $q_{br}(i, j) = q_{br}^b(i, j) + q_{br}^f(i, j)$  is calculated. According to the bank erosion rate, each boundary node is moved the distance of  $\Delta B_{1,j}$

$$\Delta B_{1,j} = \varepsilon_{1,j} \Delta t_{bank} \quad (41)$$

where  $\Delta t_{bank}$  is the bank erosion time step. In Figure 2,  $(1', j)$  and  $(1', j + 1)$  are the boundary nodes after bank erosion, and the hatched area represents the eroded material. At the inlet section, the bank erosion rate is assumed to be zero. At the outlet section, the bank erosion rate is assumed to be the same as in the adjacent upstream section.

### Mesh-adjustment algorithm

After obtaining the erosion distance at each boundary node, the new boundary lines (dark solid line in Figure 3) are obtained. Since the boundary of the computational domain is changing, the mesh must be adjusted from time to time. The dynamic mesh traces the boundary of the meandering channel and matches the computational domain to the new channel. The new mesh for the next time step is equally spaced along the banks and is also equally spaced in the transverse direction.

In Figure 3, open dots represent the old boundary nodes, and solid dots represent the boundary nodes after the banks are moved according to the erosion distance. Solid squares represent the boundary nodes after the mesh is adjusted. In this figure, node  $A$  retreats, and node  $B$  advances. The old cross-section  $AB$  is moved to  $A'B'$  after bank erosion occurs. Assuming that the channel width remains unchanged during the meandering process, bank retreat at one side of the channel should be equal to the advance at the other side of the channel. In these channel-meandering simulations, the bank erosion rate is the average of the rates at both banks of the channel because a constant channel width is assumed.

The new centreline is obtained by connecting the centres of each new cross-section. For example, the centre of cross-section  $A'B'$  is the point  $C'$ . The new centreline may be somewhat longer or shorter than the previous centreline due to deformation of the meandering loops. Because no additional nodes are added or deleted during computation, the position of each cross-section should be relocated to obtain a mesh for better computational accuracy and efficiency. The new centreline is equally divided, and the centre of each cross-section is relocated. For example, the dashed line in Figure 3 represents the new centreline. Open squares represent the centres of the new cross-sections after the equal division.  $C''$  is the new centre of the old cross-section  $AB$ . Points  $C'$  and  $C''$  are usually quite close

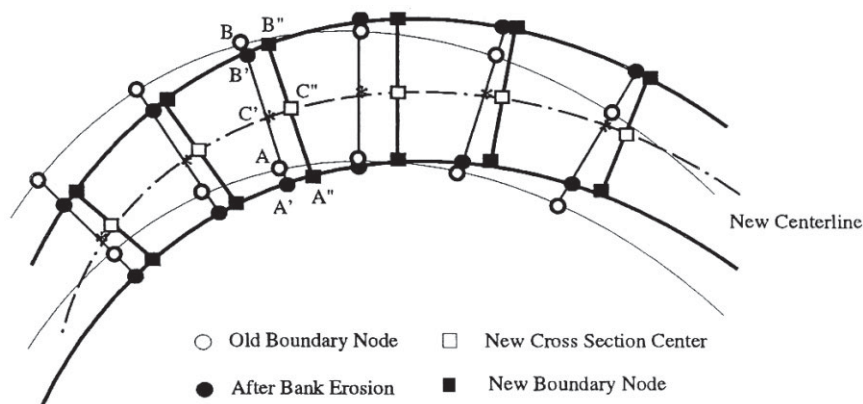


**Figure 3.** Adjustment of channel boundaries.

because the bank is only restricted to move a distance of less than 2 per cent of the channel width at each time step. In the case of a high erosion rate, the time step of bank erosion must be reduced. The adjusted cross-section  $A''B''$  must be normal to the new centreline at  $C''$  and have a width equal to the initial channel width  $AB$ . Then, for each cross-section, computational nodes along the transverse direction are uniformly distributed. The adjusted mesh has the same computational domain as the previous one, even though the positions of cross-sections and computational nodes have been relocated in the physical domain. Each new cross-section of the adjusted mesh is normal to the new centreline, and computational nodes are uniformly distributed along the transverse direction.

Since the computational nodes do not move considerably in each time step, bed elevation at any node in the new mesh is interpolated according to the bed elevation of the adjacent upstream and downstream nodes in the old mesh. After the mesh is adjusted, the flow field must be recalculated for a certain time to achieve a steady state in the new channel. This entire process is repeated for each new morphological time step until the simulation is completed at the specified time step. Since boundary nodes move less than 2 per cent during each time step, the error due to interpolation is assumed negligible.

### Test and Verification

Friedkin (1945) conducted a series of experimental studies to examine the processes whereby meanders are formed, and the relationships of meander formation to water discharge, sediment load, bank composition and valley slope. In the present study, the Friedkin (1945) experimental case involving initiation of the meandering process was simulated where a straight channel having a single meandering loop at the inlet was developed into a meandering channel. In his experiment, a constant discharge of 1.416 l/s was introduced at the inlet. The initial cross-section was trapezoidal with a top width of 25.96 cm and a bottom width of 17.37 cm. About one-third of the initial bend had a non-erodible rigid wall. Bed sediment was relatively uniform with a mean size of 0.45 mm. Bank material and bed material were uniform, homogenous, and non-cohesive. After three hours, a meandering channel was formed (shown in Figure 4). The results were repeated in a subsequent run where the same number of meandering loops having similar magnitude and wavelength were produced.

In this simulation, a two-dimensional, computational mesh is generated for the original planform. Flow discharge is specified as a constant at the inlet. The discharge of suspended and bedload sediment at the entrance section is equal to the transport capacity of bedload and suspended load. The boundary roughness height equals the mean particle size, and the water surface elevation at the outlet cross-section remains constant. For the simulation, the banks of the upper third of the first bend are fixed. The outlet cross-section is set parallel to the immediate upstream cross-section, allowing the outlet cross-section to rotate around its centreline. In this simulation, a constant channel width is maintained by averaging the rates of bank erosion at both banks.

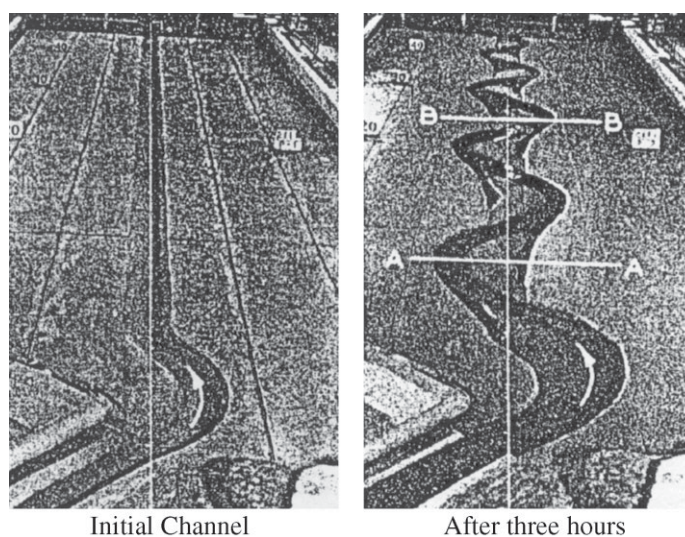


**Figure 4.** Photo of experimental result.

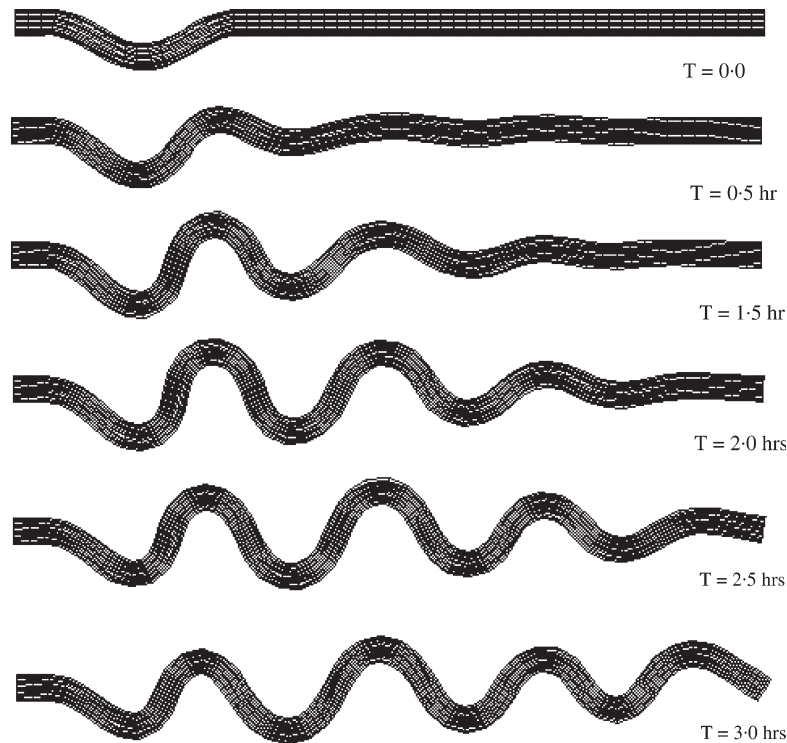


**Figure 5.** Changes in computational meshes during the meander-forming processes.

Adjustments to the computational meshes made during the simulation are plotted in Figure 5; the top diagram illustrates the original mesh, and the bottom one illustrates the mesh of the completely developed meandering channel. The present model requires the total number of cross-sections and nodes in each cross-section to remain unchanged, so the distance between cross-sections increases as the channel length increases. In this model run, the initial aspect ratio of the finite element mesh is 1:4, and the aspect ratio of the developed meandering channel is 1:7, which satisfy the convergence criteria for the hydrodynamic model (Duan, 2004). After each mesh adjustment, the flow field is recalculated as the initial condition by using flow solutions from previous time steps.

The simulated flow field is plotted in Figure 6. It includes the flow velocity vector, and surface elevation occurring during the meander-forming process. The flow depth is very shallow, and velocity is low in areas outside the computational domain; consequently, the present model assumes that sediment transport in these areas is negligible. At the beginning of the simulation ( $T = 0$  h), the initial meandering loop causes a redistribution of flow momentum. As time progresses, sand bars develop near the inner bank of the initial loop and at the location where the initial loop connects with the straight reach. At  $T = 0.5$  h the primary flow course becomes wave-like because sand bars form in the straight reach. This wave-like flow pattern facilitates the development of sand bars, and at  $T = 2.0$  h, a fully developed meandering loop occurs in the straight reach. Two additional meandering loops are fully developed at  $T = 3.0$  h.

High-velocity zones are observed near the inner bank at the beginning of the simulation. These zones gradually shift to the outer bank as the transverse bed slope increases due to the presence of sand bars. Parker (1984) and Dietrich and Smith (1983) attributed this phenomenon to the secondary flow generated by bed topography. Simulation results indicate that the initial meandering loop propagates downstream through the formation of sand bars, resulting in a meandering flow path. Apparently, because of the uniform bed and bank material, the initial bend can be transmitted almost perfectly downstream, producing a series of uniform bends. After the meandering process reaches equilibrium, a series of almost identical sand bars resides on the inside of bends.

The simulated bed elevations for the stages in the meandering process are plotted in Figure 7. Simulation results show that the generation of alternate bars occurs at both sides of the channel. The channel begins meandering after the alternate bars are formed. As time progresses, the meandering amplitude and wavelength increase gradually. Friedkin (1945) states that bends develop as flow impinges on the bank and erodes bank material, then deposits the material on the inside of the bend. Super-elevation on concave banks of this low-sinuosity stream is observed in the experiment.



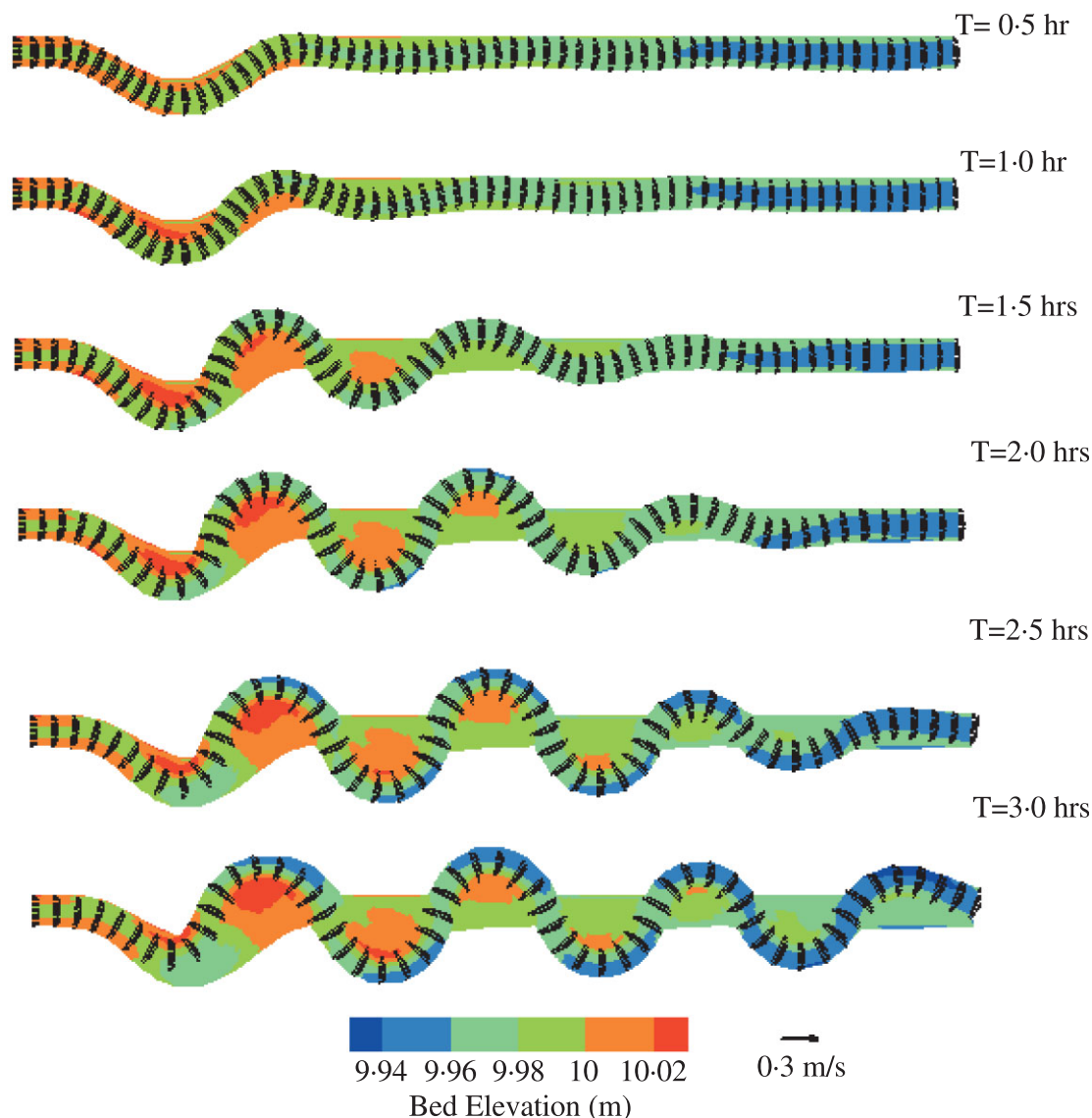


**Figure 6.** Simulated flow field including velocity and surface elevation. This figure is available in colour online at [www.interscience.wiley.com/journal/espl](http://www.interscience.wiley.com/journal/espl)

Super-elevation of flow near the concave bank increases as the meandering process evolves, indicating that secondary flow becomes stronger as sinuosity increases. The amplitude and wavelength of the formed meandering stream are very close to experimental observations as shown in Figure 4.

Longitudinal profiles representing the various stages in the meandering process at the inner, outer and centreline locations are plotted in Figure 8. This observation is verified by numerous field observations where the slope of alluvial channels decreases as meandering develops. Because the cross-sections are deep along the concave banks of the bends and shallow in the crossings between the bends (plotted in Figure 9), the longitudinal profiles at the centreline consist of a series of deep, separated by shallow, crossings. At the apex where the concave bank exists, triangular-shaped cross-sections are formed (Figure 9), which agrees very well with field measurements (e.g. Julien, 2002; Julien and Anthony, 2002).

Sediment, including suspended load and bedload, was fed at the entrance. The simulation shows that sediment from bank erosion replenishes sediment deposited on sand bars. Trading sediment from the main channel with sediment from bank erosion consequently results in downstream aggregation. In the present study, we also observed that the

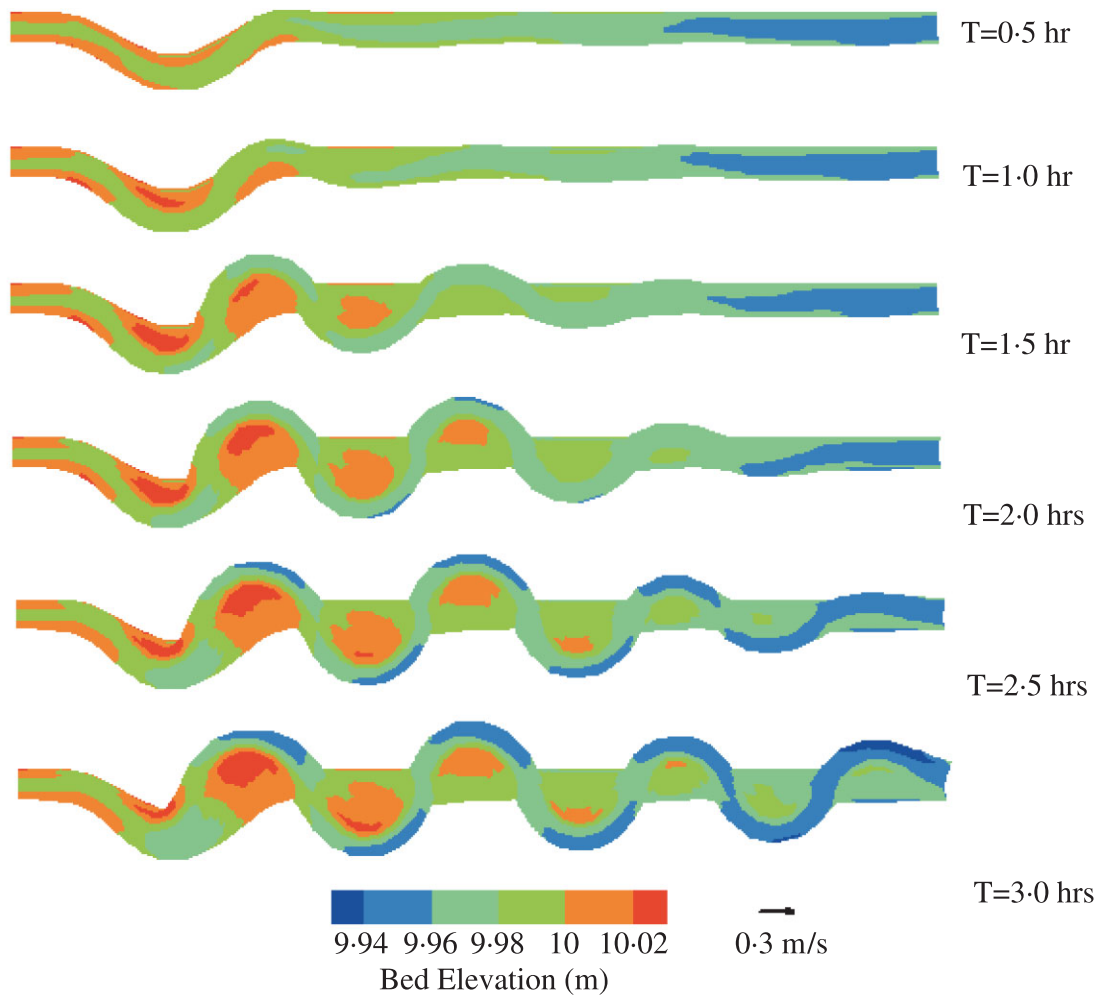


**Figure 7.** Initiation of a meandering channel from a straight channel. This figure is available in colour online at [www.interscience.wiley.com/journal/espl](http://www.interscience.wiley.com/journal/espl)

differences between bed elevations at the inner and outer banks increase with the formation of meandering channels, which indicates that the transverse bed slope increases as the meandering process evolves.

The simulated meandering planform and cross-sections are very close to the experimental results. This indicates that the present model is capable of predicting the formation of alternate bars from a single perturbation in a straight reach of a channel. This two-dimensional model also adequately simulates the initiation of channel meandering.

## Discussion

An example from the Rio Puerco in New Mexico is shown in Figure 10. Accordingly, a straight channel was excavated with a vertical drop (about 2 m) in sandstone in order to prevent lateral migration and eventual impingement of the channel into the nearby road embankment. The elevation drop triggered a slight lateral perturbation of the system and the downstream portion of the channel started to meander. The features of the channel shown in Figure 10 are quite similar to the features obtained by the model. Essentially, the amplitude of meandering decreases in the downstream direction. The resulting channel features are very similar to those described by the model in Figure 7.

Natural meandering streams commonly have cohesive banks (Knighton and Nanson, 1993; Millar, 2000). Retreat of cohesive bank lines is a complex process consisting of fluvial erosion, bank failure, weathering, piping or sapping. Bank failure can dominate bank erosion processes involving cohesive bank material, and algorithms for mass failure are available for cohesive banks (Darby and Delbono, 2002). Bank failure models for cohesive bank material, such as

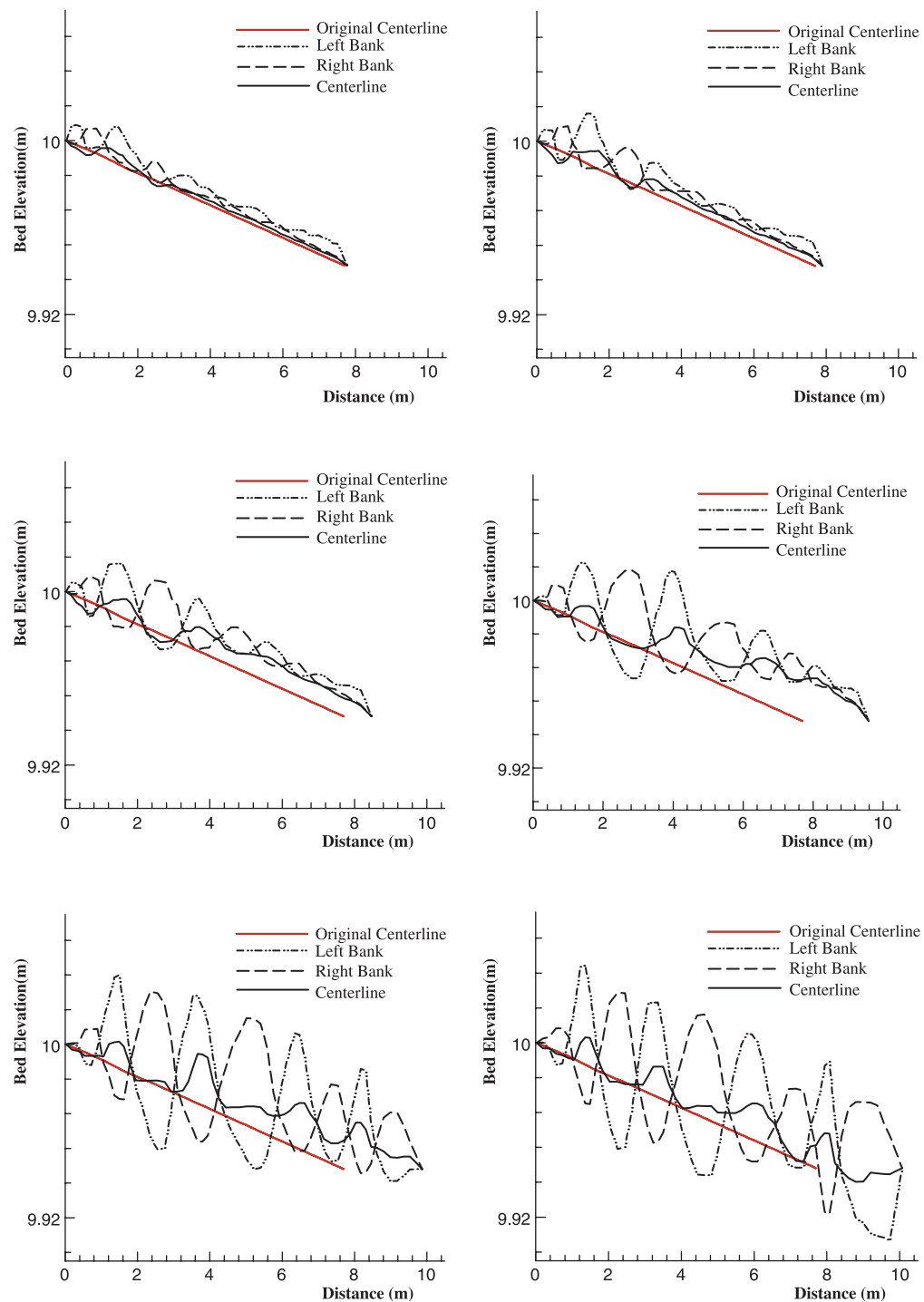


**Figure 8.** Changes in longitudinal bed slopes with time. This figure is available in colour online at [www.interscience.wiley.com/journal/espl](http://www.interscience.wiley.com/journal/espl)



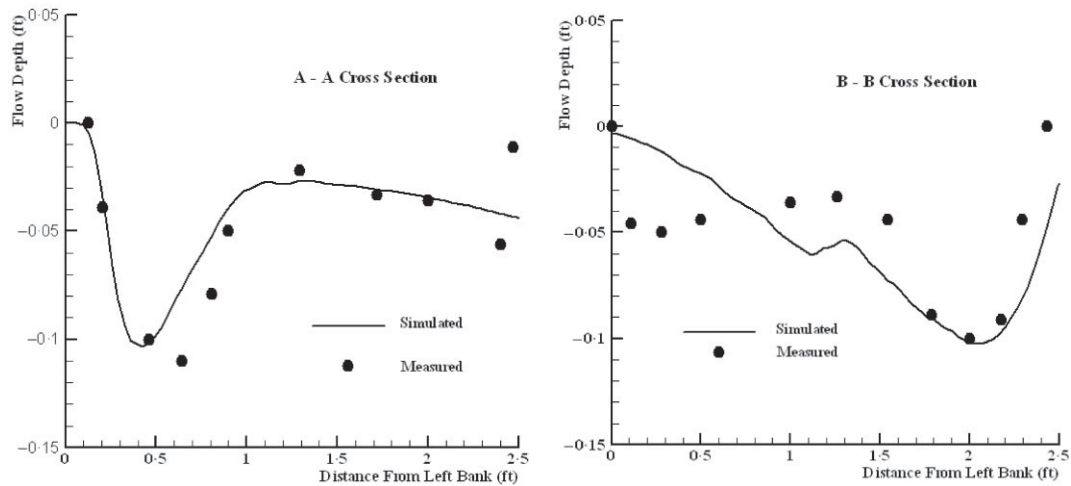


**Figure 9.** Comparison of simulated and measured cross-sections.



**Figure 10.** Photo of the Rio Puerco downstream of a perturbation. This figure is available in colour online at [www.interscience.wiley.com/journal/espl](http://www.interscience.wiley.com/journal/espl)

planar models (Osman and Thorne, 1998; Darby and Thorne, 1996), rotational models or cantilever models, can be used instead of Equation 36. Bank failure is a probabilistic phenomenon with a frequency relating to the frequency of river flood flow that can be approximated with a LP(3) distribution (Duan, 2001). The mass volume from bank failure is estimated as a function of bank geometry, properties of bank material, and frequency of bank failure.

## Conclusions

The present study incorporates the physically based bank erosion model into the mass conservation equation to predict the rate of bank line advance or retreat. The bank erosion model combined with a two-dimensional hydrodynamic model replicates Friedkin's laboratory experiments on the formation of meandering streams. An important aspect of this model is that bank erosion does not guarantee the retreat of a bank line if eroded bank material remains at the toe of the bank. Whether or not a bank retreats or advances depends on the balance of sediment load at near-bank regions where sediment may come from upstream, bank erosion, and secondary flow. The strength of secondary flow in redirecting bedload transport correlates with the local radius of curvature as well as sinuosity of meandering channels. Modelling results clearly demonstrated the evolution of meandering from perturbation. The resulting meandering

channel has almost uniform loops, and the location and size of the sand bars are similar to the experimental observations. The essential processes leading to meander formation are well replicated with this model. Additionally, modelling results also indicated that suspended sediment is less important in modelling meander migration, while bank erosion and bedload transport play significant roles in the meandering evolution process. The growth of sand bars determines the hydrodynamic flow field that pushes towards the concaving banks. Bank material from the caving banks will supplement sediment deposits on point bars when bed and bank material are the same, such as in the laboratory experiments. At this point, this model properly simulates key laboratory experiments of channel meandering. It is also very similar to some features observed in the field, such as observed on the Rio Puerco in New Mexico. This model enhances the current capability in modelling natural morphodynamic processes. This also contributes to better understanding of the processes of lateral channel migration and helps explain the formation of river meanders.

### Acknowledgements

This work is a result of research sponsored by the US Department of Defense Army Research Office under Grant Number DAAD19-00-1-0157, and by a Cooperative Agreement between the US Army Corps of Engineers and Desert Research Institute (DRI), under Grant Number DACW42-03-0-0003. Thanks to Ms Jennifer Lease for her help in proofreading this manuscript.

### References

- ASCE Task Committee. 1998. River width adjustment. I: Processes and mechanisms. *Journal of Hydraulic Engineering* **124**(9): 881–902.
- Bormann N, Julien PY. 1990. Scour downstream of grade-control structures. *Journal of Hydraulic Engineering* **117**(5): 579–594.
- Bridge JS. 1992. A revised model for water flow, sediment transport, bed topography and grain size sorting in natural river bends. *Water Resources Research* **28**: 999–1013.
- Chien N, Wan ZH. 1991. *Dynamics of Sediment Transport*. Academic Press of China: Beijing 563–576; (in Chinese).
- Crosato A. 1990. Simulation of meandering river processes. In *Communications on Hydraulic and Geotechnical Engineering*. Delft University of Technology: Delft, The Netherlands.
- Darby S, Delbono I. 2002. A model of equilibrium bed topography for mean bends with erodible banks. *Earth Surface Processes and Landforms* **27**(10): 1057–1085.
- Darby SE, Thorne CR. 1996. Development and testing of riverbank-stability analysis. *Journal of Hydraulic Engineering* **122**(8): 443–454.
- Darby SE, Alabyan AM, Van De Wiel MJ. 2002. Numerical simulation of bank erosion and channel migration in meandering rivers. *Water Resources Research* **38**(9): 1163. DOI: 10.1029/2001WR000602
- Dietrich W, Smith JD. 1983. Influence of the point bar on flow through curved channels. *Water Resources Research* **19**: 1173–1192.
- Duan JG. 2001. Simulation of streambank erosion processes with a two-dimensional numerical model. In *Landscape Erosion and Evolution Modelling*, Harmon RS, Doe WW III (eds). Kluwer Academic/Plenum Publishers: New York; 389–427.
- Duan JG. 2004. Simulation of flow and mass dispersion in meandering channels. *Journal of Hydraulic Engineering* **130**(10): 964–976.
- Duan JG, Wang SSY, Jia Y. 2001. The application of the enhanced CCHE2D model to study the alluvial channel migration processes. *Journal of Hydraulic Research* **39**(5): 469–480.
- Engelund F. 1974. Flow and bed topography in channel bend. *Journal of Hydraulic Division* **100**(11): 1631–1648.
- Friedkin J. 1945. *A Laboratory Study of the Meandering of Alluvial Rivers*. US Waterways Experiment Station: Vicksburg.
- Hooke JM. 1995. River channel adjustment to meander cutoffs on the River Bollin and River Dane. *Geomorphology* **14**: 235–253.
- Ikeda S. 1989. Sediment transport and sorting at bends. In *River Meandering*, Ikeda S, Parker G (eds). American Society of Civil Engineers: New York; 103–115.
- Ikeda S, Parker G, Sawai K. 1981. Bend theory of river meanders, 1, Linear development. *Journal of Fluid Mechanics* **112**: 363–377.
- Ikeda S, Nishimura T. 1986. Flow and bed profile in meandering sand-silt rivers. *Journal of Hydraulic Engineering* **112**(7): 562–579.
- Johannesson H. 1985. *Computer Simulation of Migration of Meandering Rivers*. Dissertation, University of Minnesota, St. Paul.
- Julien PY. 2002. *River Mechanics*. Cambridge University Press: Cambridge.
- Julien PY, Anthony DJ. 2002. Bedload motion and grain sorting in a meandering stream. *Journal of Hydraulic Research* **40**(2): 125–133.
- Kikkawa H, Ikeda S, Kitagawa A. 1976. Flow and bed topography in curved open channels. *Journal of Hydraulic Division* **102**(9): 1327–1342.
- Knighton AD, Nanson GC. 1993. Anastomosis and the continuum of channel pattern. *Earth Surface Processes and Landforms* **18**: 613–625.
- Lan YQ. 1990. *Dynamic Modelling of Meandering Alluvial Channels*. Dissertation, Colorado State University, Fort Collins.
- Lancaster ST, Bras RL. 2002. A simple model of river meandering and its comparison to natural channels. *Hydrological Processes* **16**(1): 1–26.
- Millar RG. 2000. Influence of bank vegetation on alluvial channel patterns. *Water Resources Research* **36**: 1109–1118.
- Mosselman E. 1998. Morphological modelling of rivers with erodible banks. *Hydrological Processes* **12**: 1357–1370.
- Nagata N, Hosoda T, Muramoto Y. 2000. Numerical analysis of river channel processes with bank erosion. *Journal of Hydraulic Engineering* **126**(4): 243–252.
- Nicholas AP, Smith GHS. 1999. Numerical simulation of three-dimensional flow hydraulics in a braided channel. *Hydrologic Processes* **13**: 913–929.

- Odgaard A. 1989a. River meander model, I: Development. *Journal of Hydraulic Engineering* **115**(11): 1433–1450.
- Odgaard A. 1989b. River meander model, II: Application. *Journal of Hydraulic Engineering* **115**(11): 1450–1464.
- Olsen NRB. 2003. Three-dimensional CFD modelling of self-forming meandering channel. *Journal of Hydraulic Engineering* **129**(5): 366–372.
- Osman MA, Thorne CR. 1988. Riverbank stability analysis. I: Theory. *Journal of Hydraulic Engineering* **114**(2): 134–150.
- Parker G. 1984. Lateral bedload transport on side slope. *Journal of Hydraulic Engineering* **110**: 197–199.
- Parker G, Andrews ED. 1986. On the time development of meander bends. *Journal of Fluid Mechanics* **162**: 139–156.
- Pizzuto JE. 1990. Numerical simulation of gravel river widening. *Water Resources Research* **26**: 1971–1980.
- Sun T, Meakin P, Jossang T, Schwarz K. 1996. A simulation model for meandering rivers. *Water Resources Research* **32**: 2937–2954.
- Sun T, Meakin P, Jossang T. 2001a. A computer model for meandering rivers with multiple bedload sediment sizes. 1. Theory. *Water Resources Research* **37**(8): 2227–2241.
- Sun T, Meakin P, Jossang T. 2001b. A computer model for meandering rivers with multiple bedload sediment sizes 2. Computer simulations. *Water Resources Research* **37**(8): 2243–2258.
- Van Rijn LC. 1989. *Sediment transport by currents and waves*. Technical Report H461. Delft Hydraulics: Delft, The Netherlands.
- Wang SS, Hu K. 1990. Improved methodology for formulating finite element hydrodynamic models. In *Finite Elements in Fluids, Volume 8*, Chung T (ed.). Hemisphere Publishing: New York; 1127–1134.